PNAS RESEARCH ARTICLE | ENGINEERING OPEN ACCESS

Confinement effects facilitate low-concentration carbon dioxide capture with zeolites

Donglong Fu[a], Youngkyu Park[a], and Mark E. Davis[a,1]

Contributed by Mark Davis; received July 5, 2022; accepted August 21, 2022; reviewed by Christopher W. Jones and Tatsuya Okubo

Engineered systems designed to remove CO_2 from the atmosphere need better adsorbents. Here, we report on zeolite-based adsorbents for the capture of low-concentration CO_2. Synthetic zeolites with the mordenite (MOR)-type framework topology physisorb CO_2 from low concentrations with fast kinetics, low heat of adsorption, and high capacity. The MOR-type zeolites can have a CO_2 capacity of up to 1.15 and 1.05 mmol/g for adsorption from 400 ppm CO_2 at 30 °C, measured by volumetric and gravimetric methods, respectively. A structure–performance study demonstrates that Na^+ cations in the O33 site located in the side-pocket of the MOR-type framework, that is accessed through a ring of eight tetrahedral atoms (either Si^{4+} or Al^{3+}: eight-membered ring [8MR]), is the primary site for the CO_2 uptake at low concentrations. The presence of N_2 and O_2 shows negligible impact on CO_2 adsorption in MOR-type zeolites, and the capacity increases to ∼2.0 mmol/g at subambient temperatures. By using a series of zeolites with variable topologies, we found the size of the confining pore space to be important for the adsorption of trace CO_2. The results obtained here show that the MOR-type zeolites have a number of desirable features for the capture of CO_2 at low concentrations.

physisorbents | carbon capture | direct air capture | adsorption sites | pore space size

The anthropogenic emission of CO_2 is associated with the continuous increase in global temperature since the industrial revolution. Therefore, many CO_2 mitigation strategies have been under investigation in the past years with the goal of net-zero emission by 2050. Point-source capture provides solutions for the sustainable operation of steel industries, cement plants, coal-based power stations, and the like. Bioenergy with carbon capture and storage (BECCS) and direct air capture (DAC) are being investigated for the direct removal of CO_2 from air to address the emissions from mobile sources such as automobiles, airplanes, and cargo ships (1, 2). BECCS and DAC provide opportunities for net-negative emissions.

The search for CO_2 adsorbents that are affordable, effective, energy efficient, environmentally friendly, and safe for large-scale applications poses a serious challenge for the implementation of carbon capture technologies (3–5). This is particularly significant for DAC because of the low diffusion rates and low CO_2 capacities resulting from trace concentrations of CO_2 (5). It is generally believed that physisorbents are not applicable to the DAC system due to the their weak affinity for CO_2 (6). Thus, chemisorbents have been extensively investigated for trace CO_2 capture (7). Liquid amine and alkaline adsorbents as well as other types of chemisorbents (e.g., ionic liquids (8) and electric based membranes (9)) have been investigated for the capture of CO_2 from low-concentration environments. However, the intensive energy requirements for desorption (60–120 kJ/mol) and slow kinetics may be problematic for processing the large quantities needed for the implementation of DAC with chemisorbents. Amines supported on porous materials have also been studied for DAC to increase surface exposure and diffusion kinetics as compared to the liquid analogs (1, 10–14). The time-dependent oxidative degradation and evaporation of amines are intrinsic challenges to the use of these methods (15). The development of new physisorbents that display high stability, low energy cost for desorption, fast sorption kinetics, and high capacity, as well as that possess moderate adsorption heat of 30–60 kJ/mol and fully reversible physisorption properties, could be enabling adsorbents for large-scale DAC (16).

The most widely studied physisorbents for DAC are metal–organic frameworks (MOFs) (5). Promising CO_2 capture performances are reported for hybrid ultramicroporous materials, a subgroup of MOFs (17–20). The high performance of these solids originates from the strongly electronegative, fluorine-based adsorption centers as well as the well-controlled pore size (20). However, it is still a challenging task to obtain a MOF sorbent for DAC with cost-effective scalability, high performance, and long-term stability (18, 20). Zeolites are another type of microporous materials with vast structural and physicochemical properties and high

Significance

Direct air capture (DAC) of CO_2 from the atmosphere is being pursued to aid in mitigating global CO_2 amounts and possibly reaching net negative emissions by 2050. We report that a type of commercialized zeolite, mordenite (MOR)-type zeolite, is a promising adsorbent for DAC because of its high CO_2 capacity, high selectivity, fast kinetics, low isosteric heat of adsorption, and high stability under simulated DAC conditions. We demonstrate that the primary site for CO_2 adsorption in the MOR-type zeolite is located at the side-pocket and that its size (i.e., the confinement effect) is the key to the performance by comparing its adsorption behavior to those obtained from a number of other zeolites with varying pore space sizes.

Author affiliations: [a]Chemical Engineering, California Institute of Technology, Pasadena, CA 91125

Author contributions: D.F. and M.E.D. designed research; D.F. performed research; D.F., Y.P., and M.E.D. analyzed data; D.F. and M.E.D. wrote the paper; and Y.P. collected NMR data.

Reviewers: C.W.J., Georgia Institute of Technology; and T.O.,The University of Tokyo.

Competing interest statement: Three US provisional patent applications (CIT 8767-P, CIT 8767-P2, and CIT 8785-P) related to this work have been applied for by D.F. and M.E.D. as co-inventors. M.E.D. is a consultant for Carbon Capture, Inc.

[1]To whom correspondence may be addressed. Email: mdavis@cheme.caltech.edu.

This article contains supporting information online at http://www.pnas.org/lookup/suppl/doi:10.1073/pnas.2211544119/-/DCSupplemental.

Published September 19, 2022.

stability. They can be synthesized in large quantities in cost-effective processes and have a long history in the industry for catalysis and adsorption (21). For carbon capture, they often possess faster kinetics than supported amines (22). These merits have made zeolites interesting candidates for the capture of high-concentration CO_2 (23–25). The known challenges for the application of zeolites for DAC are the detrimental effect of water as well as capacities for low-concentration CO_2 capture. The former issue can be addressed by engineering multibed systems with a desiccant bed upstream of the zeolitic adsorbents (26). For DAC applications, the capture of atmospheric water could be a useful endeavor to complement the removal of CO_2 in areas where fresh water is badly needed. To address the later issue, recent research has been focused on maximizing the number (22, 27) of adsorption sites by using low-silica zeolites or adjusting the type of extraframework cations (28–30) by incorporating Zn^{2+} and Ca^{2+} ions. These approaches have given high capacities of 0.4 and 0.87 mmol/g for Na-FAU zeolites with Si/Al = 1.2 (zeolite X) and 1.0 (low-silica zeolite X), respectively, as well as 0.67 mmol/g for Zn-CHA with Si/Al = ∼2.0 and 1.8 mmol/g for Ca-LTA with Si/Al = 1 (the three letter codes of zeolites are assigned by the Interantional Zeolite Association for indicating their framework topologies). However, the low thermostability for low-silica zeolites and irreversible adsorption of CO_2 in Ca^{2+}-containing zeolites will probably present challenges for commercial-scale implementation of DAC. Therefore, there remains a need for a zeolitic adsorbent with competitive capacity, high stability, and cyclability (31, 32).

In this work, we report that the confinement effect in zeolites greatly affects the adsorption of low-concentration CO_2. MOR-type zeolites with eight-membered ring (8MR) side-pockets synthesized with or without (33) organic structure-directing agents (OSDAs) can give a CO_2 capacity of ∼1.15 mmol/g, among the highest reported for physisorbents for DAC. This capacity results in approximately an order of magnitude improvement of adsorption efficiency (i.e., CO_2 per adsorption site), compared to the standard 13X zeolite adsorbent. The O33 site in the 8MR side-pocket is the primary adsorption site of MOR-type zeolites, and the size of the confined space for the adsorption site in zeolites dictates their properties for the adsorption of 400 ppm CO_2.

Results and Discussion

MOR-Type Zeolites for Capture of Low-Concentration CO_2. The MOR-type zeolite framework (Fig. 1*A*) possesses unidirectional 12-membered ring (12MR, 7.0 × 6.5 Å^2) channels. The smaller 8MR channels with elliptical openings (5.7 × 2.6 Å^2) run in parallel and are interconnected to the 12MR to create a side-pocket with 8MR windows (4.8 × 3.4 Å^2). This zeolite has been shown to be an interesting catalytic material, with greatly

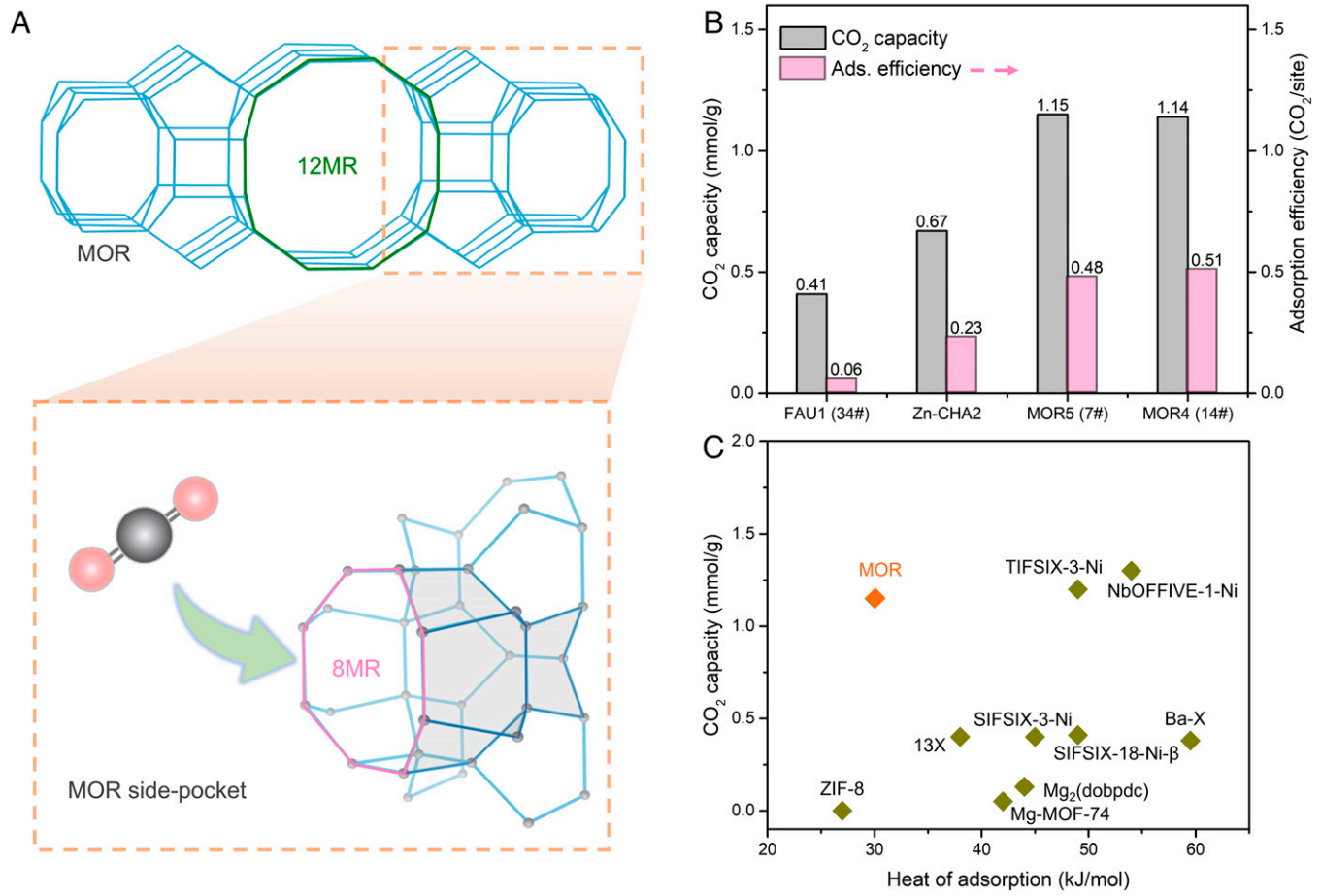

Fig. 1. Performance of MOR-type zeolites for the capture of 400 ppm CO_2. (*A*) MOR-type framework with the 12MR channel and 8MR side-pocket highlighted in green and pink, respectively. Straight line segments represent bridging oxygen atoms, and their intersection points the tetrahedral atoms (Si or Al). The arrow indicates the adsorption of CO_2 molecules in the 8MR side-pocket. (*B*) Capacities for CO_2 adsorption in Na^+ form of MOR-type (MORa) zeolites, where *a* indicates the measured Si/Al ratio. Sample codes in the bracket are listed in *SI Appendix*, Table S1. 13X and Zn-CHA (28) are used as references. Note that Zn^{2+} was the adsorption site for Zn-CHA2, while Na^+ was used for the other zeolites. (*C*) Comparison of the 400 ppm CO_2 capture capacity of MOR-type zeolites (7#) with other types of physisorbents with moderate adsorption heat of 25–60 kJ/mol. Data were taken from the literature for, ZIF-8 (18), 13X (18), SIFSIX-18-Ni (18), SIFSIX-18-Ni-β (18), NbOFFIVE-1-Ni (6), Mg_2(dobpdc) (13), Mg-MOF-74 (18), and Ba-X(29).

different performance in the two types of zeolite channels observed for reactions due to their respective local environments (34–37). The Iglesia and Bao groups reported that the proton sites used for acid catalysis located in the 8MR side-pocket selectively catalyze the carbonylation of dimethyl ether (34) and the ketene-mediated syngas-to-ethylene reactions (37), respectively. The MOR-type zeolite has been reported for the flue gas capture (38). MOR-type zeolites have also shown potential to adsorb a number of different components in the gas phase when they are at low concentration, including NO_2 (39) and N_2O (40). However, no details are available for the sites for adsorption. As shown below, the side-pocket of MOR-type zeolites can provide sites that are able to capture low concentrations of CO_2.

A series of MOR-type zeolites (*SI Appendix*, Table S1) was prepared from commercially available samples and those that we synthesized (*SI Appendix*, Figs. S1 and S2) (41, 42). The equilibrium capacities were obtained from CO_2 isotherms (*SI Appendix*, Figs. S3 and S4) measured at 25 °C. The distributions of Na^+ cations (*SI Appendix*, Table S1) in the two channels of the MOR framework locations can be determined by deconvoluting the OH stretching region of the Fourier transform infrared spectra (FTIR; *SI Appendix*, Fig. S5) (37). The CO_2 capacity increases with the number of Na^+ cations in the 8MR side-pockets (*SI Appendix*, Fig S6). The highest CO_2 capacity (Fig. 1*B* and *SI Appendix*, Table S2 and Fig. S4) obtained is 1.15 mmol/g for MOR (7#) that has a Si/Al ratio of 5, with an improvement in adsorption efficiency (0.48 CO_2/Na^+) compared to 13X zeolite (0.06 CO_2/Na^+). The capacity of MOR (7#) is also about two-fold of that of the recently developed Zn-CHA adsorbent by our group (28). We successfully synthesized an OSDA-free MOR-type zeolite (14#) with slightly higher Al content (Si/Al = 4) that gave a capacity of 1.14 mmol/g (Fig. 1*B* and *SI Appendix*, Figs. S4 and S7), comparable to the value obtained from the OSDA-directed material (7#). Gravimetric measurements (*SI Appendix*, Fig. S8) of MOR-type (7#) show a capacity of 1.05 mmol/g and faster adsorption and desorption kinetics for MOR-type zeolites than those for 13X. Additionally, the sharper breakthrough curve (*SI Appendix*, Fig. S9) observed for MOR-type zeolites compared to that of 13X further confirm the faster kinetics of the former material. FTIR results (*SI Appendix*, Fig. S10) demonstrated that CO_2 molecules are exclusively physiosorbed in the MOR-type zeolites from 400 ppm CO_2. Consistent with the FTIR results, the calculated isosteric heat of adsorption (*SI Appendix*, Figs. S11 and S12) of the MOR-type (7#) zeolite is ∼30 kJ/mol, thus providing a nice compromise between 400 ppm CO_2 capture capacity and the required heat for regeneration (Fig. 1*C*).

Adsorption Sites in MOR-Type Zeolites. Studies were performed to identify the active sites responsible for the adsorption of low-concentration CO_2 in MOR-type zeolites. MOR-type (4#) zeolites were modified with pyridine, denoted as py-MOR, to selectively block the adsorption sites in the 12MR channel as well as the intersection between the 12MR channel and 8MR side-pocket (*SI Appendix*, Fig. S13). The pyridine molecule is too large to enter the 8MR (41), and it does not show CO_2 adsorption under ambient conditions (43). Interestingly, ∼85% capacity was obtained for py-MOR-type zeolites compared to the fresh MOR-type zeolites (Fig. 2*A* and *SI Appendix*, Fig. S14). These data demonstrate that CO_2 molecules in the low concentration range adsorb primarily in the 8MR side-pocket of the MOR framework. Isotherms (Fig. 2*B*) show a two-step uptake for CO_2 in Na-MOR-type zeolites with an inflection at ∼0.0001 bar, while no apparent change is observed in 13X zeolite. This behavior is probably due to the switch of adsorption cages in the MOR framework. Similar results have been reported for argon (Ar) adsorption in zeolites with multiple accessible cages (44). Although the structural changes in structure-flexible zeolites can cause two-step uptake in isotherms, the inflection pressure is highly temperature-dependent (23, 45). The MOR-type zeolite (*SI Appendix*, Fig. S15) shows constant inflection pressure at different temperatures. Furthermore, the ratio of the capacity at 0.0001 bar to that at 0.0004 bar (corresponding to 400 ppm; Fig. 2*B*) is ∼80%, comparable to the 85% obtained from pyridine shielding experiments (Fig. 2*A*). This result is consistent with the interpretation that the inflection results from the switch of adsorption cages. The data when taken together demonstrate that CO_2 molecules preferentially adsorb in the 8MR side-pocket of the MOR framework when the CO_2 is in the low-pressure range.

To better understand the structural features and the active adsorption sites that provide the adsorption performance of MOR-type zeolites, a series of Na-MOR-type samples (*SI Appendix*, Figs. S16–S19 and Tables S3 and S4) were prepared with fixed Si/Al ratio and Na^+/U.C. ranging from 0 to 5.81, where Na^+/U.C. denotes the number of Na^+ cations per MOR unit cell. As shown in Fig. 2*C*, CO_2 adsorption occurs in three stages as Na^+/U.C. varied. Specifically, CO_2 capacity slightly increases before a sharp increase occurs starting at ∼1.89 Na^+/U.C., followed by a constant value from 4.8 Na^+/U.C. Generally, monovalent Na^+ species is the only form of cation present in Na exchanged zeolites. Therefore, the distinct stages observed in these experiments result from the microenvironment of the Na^+ cations (i.e., dependent on their positions in the MOR-type framework). FTIR spectra (*SI Appendix*, Fig. S20 and Table S5) were recorded to track the adsorption state of CO_2 as a function of Na^+ loadings. Only gas phase CO_2 with vibrations at 2,348 cm^{-1} was found for stage I, consistent with the observed low capacity. With an increase of Na^+ density, a shoulder at 2,359 cm^{-1} evolved on the left side of the gas phase vibration, suggesting that CO_2 molecules physiosorbed linearly. Importantly, in the second stage, an extra band attributed to the Na-O vibration was observed between 2,400 and 2,430 cm^{-1}, indicating the close interaction between the extraframework Na^+ cation and the O atom of CO_2 molecules (46).

Single-crystal X-ray diffraction (XRD) analysis was performed with synthetic large MOR crystals (*SI Appendix*, Fig. S21) to locate the Na^+ in the MOR-type framework. Representative samples with Na^+ densities of 0.88, 2.59, 4.38, and 5.96 Na^+/U.C. were evaluated (*SI Appendix*, Table S6), corresponding to the samples highlighted as a, b, c, and d in Fig. 2*C*. The structure was solved with an orthorhombic *Cmcm* space group with lattice parameters of a typical MOR unit cell: *a*, 18.094 Å; *b*, 20.516 Å; and *c*, 7.524 Å. The refinement gave a chemical formula of $Na_xSi_{40.6}Al_{7.4}O_{96}$, where *x* denotes the number of Na^+ cations detected per MOR unit cell. The results (Fig. 2*D* and *SI Appendix*, Fig. S22 and Tables S7–S10) show that Na^+ preferentially sits in the 8MR pockets followed by the 12MR main channels. Specifically, the Na^+ cations located primarily at the center of the 8MR window inside the side-pocket at stage I with an average distance of Na1-O = ∼3.2 Å (sample a), while Na^+ cations started siting in the O33 site connecting to T3 (Na2-O33 = ∼2.7 Å) at stage II (sample b). As the CO_2 capacity sharply increases at stage II, it can be concluded that O33 site is responsible for the adsorption of low-concentration CO_2. Similarly, Boronat et al. (47) demonstrated that the O33 site is active for the selective carbonylation of dimethyl ether as it stabilizes the adsorbed methoxy species. Interestingly, the CO_2

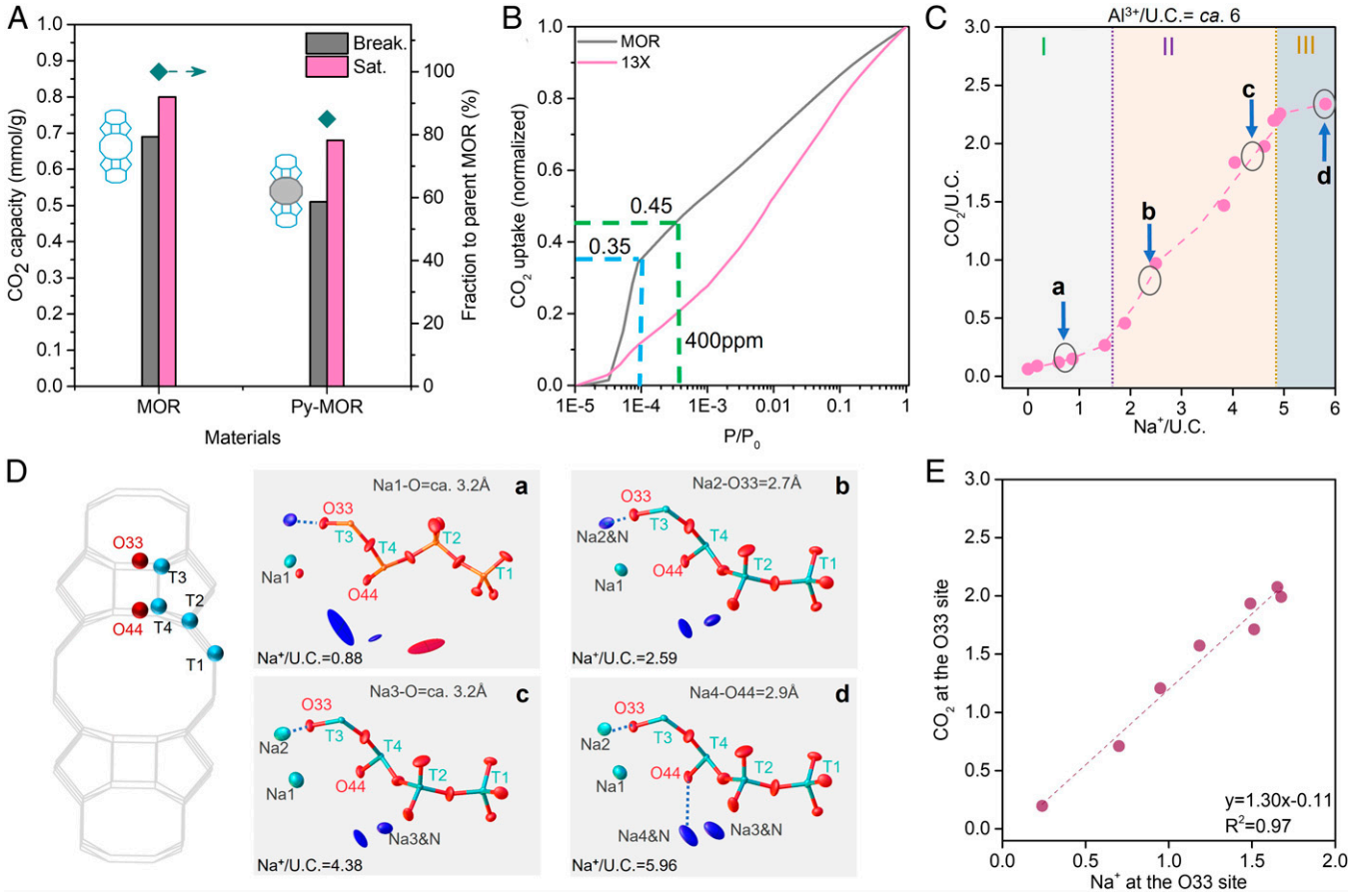

Fig. 2. Identification of adsorption sites in MOR-type zeolites. (*A*) Bar graphs of breakthrough and saturation capacities from MOR6 (4#) at 30 °C before and after pyridine modification, denoted as MOR and py-MOR, respectively. (*B*) Normalized CO_2 adsorption isotherms of MOR- and FAU-type zeolites with logarithm relative pressure. (*C*) CO_2 molecules adsorbed per MOR unit cell (CO_2/U.C.) as a function of Na^+ cation loading density (Na^+/U.C.). Note that each MOR unit cell possesses ~6 exchangeable sites (i.e., Al^{3+}). (*D*) Four T-sites (*Left*) and visualization (*Middle* and *Right*) of the positions of Na^+ in the MOR framework as a function of Na^+ loading. Labels (*a-d*) are the results from samples shown in Fig. 2*C*. Oxygen, Na^+, and N from NH_4^+ are highlighted in red, light green, and blue, respectively. Oxy denotes the oxygen atom connected to Tx and Ty sites. The distances between Na and O for Na1 and N3 are determined by their average distances to the surrounding O, as Na1 and Na3 are located at the center of 8MR windows. Na2 and Na4 are attached to O33 and O44, respectively. (*E*) Correlation of the number of CO_2 molecules adsorbed and the Na^+ cations loading in the O33 site in the 8MR side-pocket per MOR unit cell.

capacity continues to increase after the O33 site is fully occupied, as shown in sample c. The material possessed Na^+ cations (Na3-O = ~3.2 Å) at the center of the 8MR window that is located in the intersection of the side-pocket and 12MR channel. These data suggest that the Na^+ cation site in this intersection also contributes to the adsorption of low-concentration CO_2, corroborating the results from py-MOR (Fig. 2*A*) and CO_2 isotherms (Fig. 2*B*). However, adding Na^+ cations that are balanced to the O44 atom site in the 12MR channel (Na4-O44 = ~2.9 Å) did not lead to an apparent increase of capacity, as shown from the data (Fig. 2 *C* and *D*) of sample d at stage III. Furthermore, quantitative analysis of the location and number of Na^+ in the MOR-type zeolites has been performed with the OH stretching region of the IR spectra and ^1H NMR spectra (*SI Appendix*, Fig. S18 and S19 and Table S4). Correlation of the number of Na^+ at the O33 site and CO_2/U.C. gives a linear relation (Fig. 2*D*) at stage II. Therefore, these results demonstrate that the confined site O33 in the 8MR side-pocket in the MOR framework is the primary site for CO_2 adsorption at low concentrations, with the intersection site contributing ~20% of the capacity.

Confinement Effects Facilitate Low-Concentration CO_2 Adsorption. Zeolites with different topologies were investigated to determine the relationship between the size of the zeolite pore space and the adsorption behavior for capturing low-concentration CO_2 (Fig. 3 and *SI Appendix*, Tables S11 and S12 and Figs. S23–S26). The uptakes of these materials were obtained from 0.0004 (equivalent to 400 ppm) or 1 bar in the CO_2 isotherms measured at 25 °C. Linde Type L (LTL)-type zeolites with a Si/Al of 3 show almost no uptake for 400 ppm CO_2 (Fig. 3 *A* and *B*). This is probably due to the fact that the window of the 8MR channel in LTL-type zeolite has an elliptical structure of 2.3 × 5.2 $Å^2$ that is too small to allow CO_2 molecules to enter. Note that the LTL-type zeolite also has a low capacity at 1 bar CO_2 (Fig. 3*C*). The mazzite (MAZ)-type zeolites with a Si/Al of 3 show a high adsorption capacity of 0.65 mmol/g for 400 ppm CO_2. Results from CO_2 adsorption testing with pyridine containing MAZ-type zeolite (*SI Appendix*, Fig. S27) show that the 8MR side-pocket of the MAZ framework is responsible for the adsorption of 400 ppm CO_2 (as observed with the MOR-type zeolites). The MFI-type (39#) zeolites show a capacity of 0.57 mmol/g, which is much higher than the 0.4 mmol/g from 13X zeolite, although the cation content (Si/Al = 12) is 8% of that (Si/Al = 1.1) for 13X (34#). Previous simulations suggest that CO_2 preferentially adsorbs in the intersection of the two channels in Na-MFI (48). The MEL-type (40#) zeolite with similar structure and comparable cation content (Si/Al = 15) to MFI-type zeolite has a larger intersection (7.7 Å) and gives a much lower uptake for 400 ppm CO_2 (*SI Appendix*, Table S12). Thus, the high capacity of MFI-type zeolites is probably attributed to the size (6.4 Å) of the intersection.

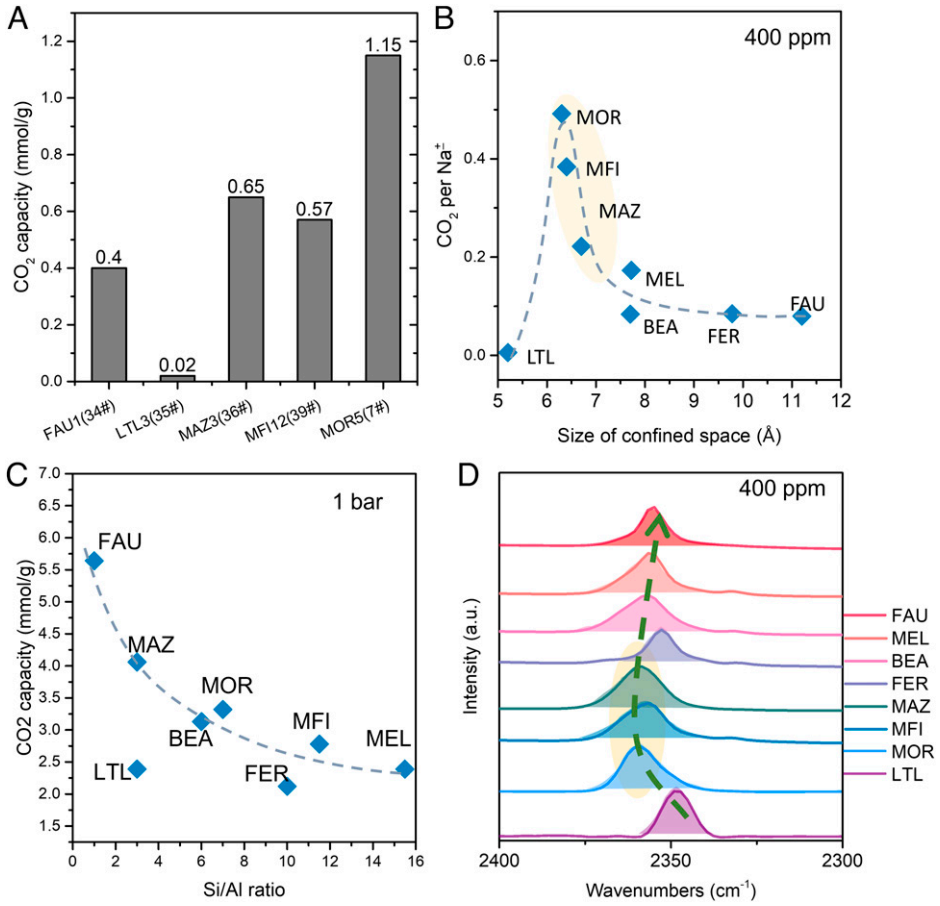

Fig. 3. Impact of the confinement effect of zeolites on CO_2 adsorption. (*A*) Capacities for 400 ppm CO_2 adsorption with the Na^+ form of zeolites with different frameworks. The three-letter framework code followed by the Si/Al ratio of the corresponding material. Sample codes in the brackets are listed in *SI Appendix*, Table S1. (*B*) CO_2 per adsorption site (i.e., Na^+) of the zeolite samples for the adsorption of 400 ppm CO_2 with increasing the size of the confined space. (*C*) Capacity of the zeolite samples for the adsorption of 1 bar ppm CO_2 with decreasing the adsorption site density/aluminum content. (*D*) FTIR spectra for the asymmetric linear vibration of CO_2 molecules in zeolites as a function of framework topology. The adsorption capacities were obtained from the isotherms measured at 25 °C. The MOR-, MFI-, and MAZ-type zeolites are highlighted in panels (*B* and *D*). The three letter codes of zeolites are assigned by the International Zeolite Association for indicating their framework topologies.

The results discussed above suggest that there are specific regions in the microporous zeolites where adsorption is preferred for capture of CO_2 from low concentrations. To further this point, the measured micropore volumes of MOR-type zeolites (49) as well as zeolites with other frameworks are consistent with the reported values. There is no apparent correlation between total micropore volume (*SI Appendix*, Table S11) and CO_2 capacity (*SI Appendix*, Table S12). However, there is a relationship between the adsorption efficiency (CO_2/Na^+) and the size of the confined space (*SI Appendix*, Text for the details of the definition of confined space, *SI Appendix*, Fig. S25) in zeolites where CO_2 molecules are preferentially adsorbed. As shown in Fig. 3*B*, the highest CO_2 adsorption efficiency obtained is from MOR-type zeolites that have a confined space of ∼6.2 Å. A decline of adsorption efficiency is observed with the increase in size of the confined space in the MFI- and MAZ-type zeolites. Further increase of the confined space leads to a fast decline of CO_2 adsorption efficiency to ∼0.1 CO_2/Al for the size >0.8 nm. The impact of cage size on the adsorption capacity for 400 ppm CO_2 has been reported for MOF materials (17). Interestingly, the adsorption performance for zeolites is distinctly different for 1 bar CO_2 and 400 ppm CO_2. These results show that the saturated CO_2 adsorption capacity at 1 bar highly depends on the total number of adsorption sites in zeolites. As shown in Fig. 3*C*, the capacity gradually decreases with the increase of Si/Al ratio in zeolites. Indeed, Pham et al. (50) have shown that the number of energetically favorable sites is decisive for adsorption of low-pressure CO_2, while CO_2 molecules at high pressure can sit in all available sites.

FTIR spectra (Fig. 3*D*) were obtained to identify the adsorption states of CO_2 in zeolites with different topologies. LTL-type zeolites showed an adsorption band at 2,348 cm^{-1}, indicating the presence of gas phase CO_2 molecules. The asymmetric vibration of adsorbed CO_2 for zeolites for MOR-, MFI-, and MAZ-type zeolites appeared at 2,357–2,360 cm^{-1}, suggesting strong ion–dipole interaction induced by the large electric field gradients in these zeolites with confined space between 6.2 and 6.7 Å (51). Interestingly, further increase of the size of the confined space resulted in a red shift of the physisorption band of the CO_2 molecules, showing a decline of electric field in the zeolites. These results demonstrate the significance of the confined space size (the confinement effect) in the adsorption of low concentration CO_2 by altering the electric gradient field, while the total density of adsorption sites dictates the adsorption of high-concentration CO_2.

MOR-Type Zeolites for DAC. Real-time breakthrough experiments were performed with the commercially available MOR-type zeolites (4#) using a stream of simulated air, which is a gas mixture of 400 ppm CO_2/1%Ar/20%O_2/N_2 at 30 °C, with Ar as the internal standard for quantitative analysis (Fig. 4*A*). A CO_2 capacity of 0.72 mmol/g was obtained with a breakthrough time of 1,839 min/g under a flow of 20 mL/min. This

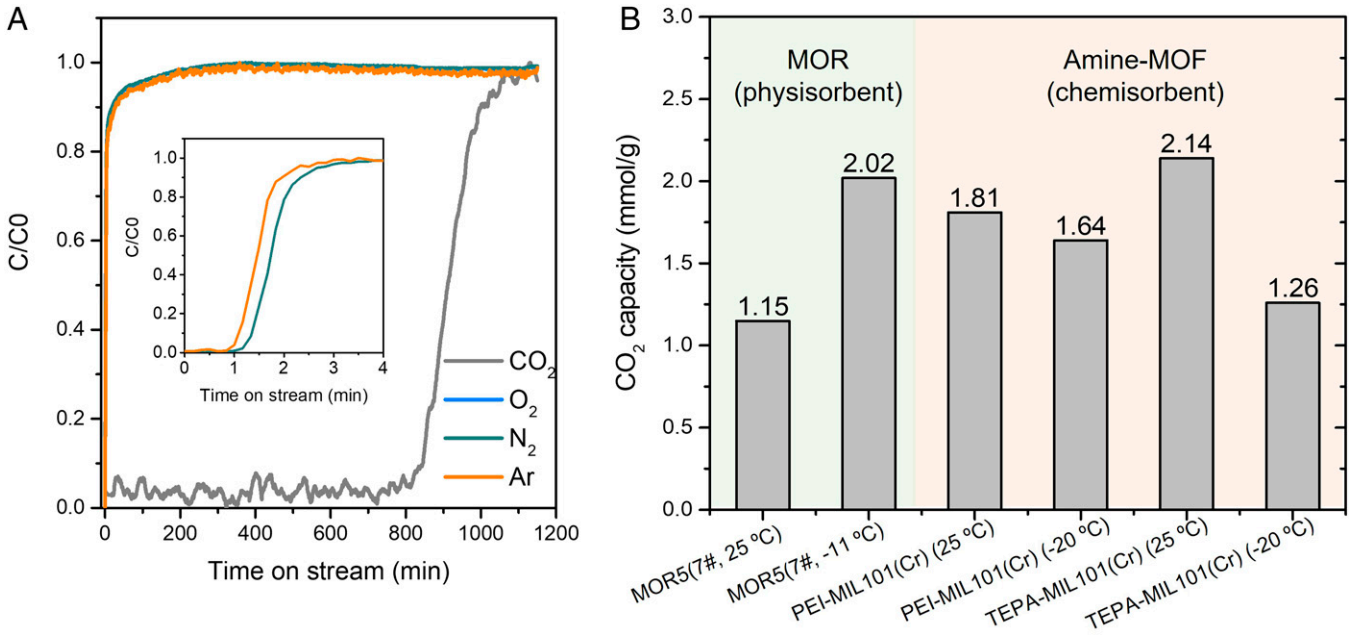

Fig. 4. Performance of MOR-type zeolites for the capture of CO_2 under simulated DAC conditions. (*A*) Real-time breakthrough profiles for MOR-type zeolites (4#) with simulated air gas of 400 ppm CO_2/1Ar% (internal standard)/20%O_2/N_2 at 30 °C. (*B*) Capacities of MOR-type (7#) zeolites for the capture of 400 ppm CO_2 at ambient and subambient temperatures, in comparison with amine-modified MOFs. Data for the amine modified MOFs were obtained from (2).

value is slightly lower than the 0.77 mmol/g obtained from the 400 ppm CO_2/He under the same conditions, which may be attributed to the weak competitive adsorption between CO_2 and N_2. The preferential adsorption of CO_2 also led to a higher CO_2/N_2 selectivity (*SI Appendix*, Fig. S28) in the breakthrough experiments with simulated air compared to the value obtained from the single-component isotherm measurements. The material is highly stable under DAC conditions, as demonstrated by the comparable CO_2 capacity obtained from six adsorption–desorption cycles with simulated air (*SI Appendix*, Fig. S29). It should be noted that the material can be fully regenerated at temperatures as low as 60 °C, which is a benefit of using pure physisorption (*SI Appendix*, Fig. S10) with the low isosteric heat of adsorption (*SI Appendix*, Fig. S12). CO_2 capacity sharply increased to 2.02 mmol/g for MOR5 (7#) at −11 °C compared to that at 25 °C (Fig. 4*B* and *SI Appendix*, Fig. S29), while a decline of adsorption efficiency/capacity was observed for chemisorbents with the increase of adsorption temperatures (2). Thus, this material may be promising for DAC under subambient temperature conditions as ∼80% of the world land temperature is lower than 25 °C (2). As with all zeolites used to date, the presence of water typically is detrimental to their CO_2 adsorption performance. As mentioned above, there are situations where the removal of water prior to CO_2 uptake can be accomplished.

Summary

MOR-type zeolites are promising physisorbents for the capture of low-concentration CO_2 (e.g., DAC). The Na^+ located at the O33 site in the 8MR side-pocket of the MOR framework is responsible for the capture of most of the 1.15 mmol CO_2/g zeolites under low-concentration conditions, and the value is among the highest obtained for physisorbents with a low isosteric heat of adsorption of ∼30 kJ/mol. The size of the confined space in the zeolite is critical to achieve high performance for the adsorption of low-concentration CO_2. MOR-type zeolites show the greatest effects from confinement. They also adsorb CO_2 with negligible impact from the presence of N_2 and O_2; the latter can cause the time-dependent degradation of amine-based adsorbents. Additionally, the capacity of the MOR-type zeolite can be further increased to over 2 mmol CO_2/g zeolite at subambient temperatures, outperforming amine-based adsorbents under those conditions as the latter shows a decline in capacity with the decrease in temperature.

Materials and Methods

Synthesis of Materials. MOR-type zeolites were synthesized from mixtures with or without organic structure directing agents. Large MOR crystals (∼40 μm) were synthesized for the single-crystal XRD analysis. The synthesis procedures for MOR-type as well as MAZ-, *BEA-, MFI-, and MEL-type zeolites can be found in *SI Appendix*. The details of the commercially obtained FAU-, FER-, LTL-, MFI-, and MOR-type zeolites can be found in *SI Appendix*.

Characterization. The crystallinity, morphology, chemical compositions, and porosity of zeolites were analyzed by powder XRD, scanning electron microscope, electron dispersive spectroscopy, and N_2 physisorption, respectively. The distribution and density of Brönsted acid sites were analyzed via FTIR and ^1H solid state magic-angle spinning NMR spectroscopy, respectively. The coordination environment of Al species in MOR-type zeolites was examined via ^{27}Al NMR spectroscopy. The locations of Na^+ cations in the MOR-type zeolites were characterized via X-ray crystallography (i.e., single-crystal XRD analysis). The detailed methods can be found in *SI Appendix*. The CIF files can be downloaded from https://data.caltech.edu/records/20259 (52).

Adsorption Performance Testing. The adsorption performance of zeolites for CO_2 was tested via both single component static adsorption and dynamic column breakthrough methods. For the single-component experiments, UHP-grade (99.999% purity) carbon dioxide was used for all adsorption measurements. CO_2 isotherms were measured on a Quantachrome Autosorb iQ adsorption. For each measurement, ∼100 mg of adsorbent was placed in a borosilicate sample cell (Type A long cell, Anton Paar) that was immersed in a liquid bath connected to a recirculating chiller with a precise temperature controller. All samples were activated prior to adsorption measurements by degassing under high vacuum at 350 °C for 6 h with a ramp rate of 1.0 °C/min.

The dynamic adsorption performance for CO_2 capture was tested via fixed bed column breakthrough experiments (28). In a typical experiment, a fixed bed was formed by loading ∼500 mg of materials into a quartz tubing (6.74 mm I.D.). The adsorbent was activated at 550 °C for 21 h under a 20 mL/min flow of 5%

Ar/He gas. Then it was cooled to 30 °C, followed by switching to the desired gas mixture for adsorption measurements at a flow rate of 20 mL/min. The gases are ~400 ppm CO_2/400 ppm Ar (internal standard)/He, 400 ppm CO_2/20 Ar% (internal standard)/N_2, or 400 ppm CO_2/1Ar% (internal standard)/20% O_2/N_2. The outlet concentrations of CO_2, N_2, Ar, and O_2 were monitored with a Ametek Dymaxion Dycor mass spectrometer. For multicycle adsorption–desorption experiments, the adsorbent was regenerated at 60 °C or 100 °C for 240 min, or 550 °C for 120 min under a 20 mL/min flow of 5% Ar/He gas. The CO_2/N_2 selectivity is defined as

$$\text{Selectivity} = \frac{q_1/q_2}{p_1/p_2},$$

where q_i and p_i denote the capacity and partial pressure of component i.

The methods for the measurement of adsorption kinetics and isosteric heat of adsorption can be found in the *SI Appendix*.

Data, Materials, and Software Availability. Crystal XRD files (.cif) data have been deposited in https://data.caltech.edu/records/20259 (52). All study data are included in the article and/or supporting information.

ACKNOWLEDGMENTS. Financial support of this work is from Carbon Capture Inc. Youngkyu Park thanks Kwanjeong Educational Foundation for financial support. The authors acknowledge Dr. Jiaxuan Li (Caltech) for writing the program for the calculation of the isosteric heat of adsorption of MOR-type zeolites and Dr. Michael K. Takase (Caltech) for his assistance with the single-crystal XRD data collection and analysis. The Beckman Institute at Caltech and Dow Next Generation Instrumentation Grant are acknowledged for support of the X-Ray Crystallography Facility and the single-crystal diffractometer, respectively.

1. E. S. Sanz-Pérez, C. R. Murdock, S. A. Didas, C. W. Jones, Direct capture of CO_2 from ambient air. *Chem. Rev.* **116**, 11840–11876 (2016).
2. G. Rim *et al.*, Sub-ambient temperature direct air capture of CO_2 using amine-impregnated MIL-101(Cr) enables ambient temperature CO_2 recovery. *JACS Au* **2**, 380–393 (2022).
3. W. Gao *et al.*, Industrial carbon dioxide capture and utilization: State of the art and future challenges. *Chem. Soc. Rev.* **49**, 8584–8686 (2020).
4. M. Ozkan, A.-A. Akhavi, W. C. Coley, R. Shang, Y. Ma, Progress in carbon dioxide capture materials for deep decarbonization. *Chem* **8**, 141–173 (2022).
5. J. Liu, Y. Wei, Y. Zhao, Trace carbon dioxide capture by metal–organic frameworks. *ACS Sustain. Chem.& Eng.* **7**, 82–93 (2019).
6. P. M. Bhatt *et al.*, A fine-tuned fluorinated MOF addresses the needs for trace CO_2 removal and air capture using physisorption. *J. Am. Chem. Soc.* **138**, 9301–9307 (2016).
7. K. S. Lackner *et al.*, The urgency of the development of CO_2 capture from ambient air. *Proc. Natl. Acad. Sci. U.S.A.* **109**, 13156–13162 (2012).
8. X. Shi, H. Xiao, K. S. Lackner, X. Chen, Capture CO_2 from ambient air using nanoconfined ion hydration. *Angew. Chem. Int. Ed. Engl.* **55**, 4026–4029 (2016).
9. H. Seo, M. Rahimi, T. A. Hatton, Electrochemical carbon dioxide capture and release with a redox-active amine. *J. Am. Chem. Soc.* **144**, 2164–2170 (2022).
10. A. Goeppert, H. Zhang, R. Sen, H. Dang, G. K. S. Prakash, Oxidation-resistant, cost-effective epoxide-modified polyamine adsorbents for CO_2 capture from various sources including air. *ChemSusChem* **12**, 1712–1723 (2019).
11. S. Choi, J. H. Drese, P. M. Eisenberger, C. W. Jones, Application of amine-tethered solid sorbents for direct CO_2 capture from the ambient air. *Environ. Sci. Technol.* **45**, 2420–2427 (2011).
12. H. Li *et al.*, Incorporation of alkylamine into metal–organic frameworks through a Brønsted acid–base reaction for CO_2 capture. *ChemSusChem* **9**, 2832–2840 (2016).
13. T. M. McDonald *et al.*, Capture of carbon dioxide from air and flue gas in the alkylamine-appended metal-organic framework mmen-Mg_2(dobpdc). *J. Am. Chem. Soc.* **134**, 7056–7065 (2012).
14. R. L. Siegelman, E. J. Kim, J. R. Long, Porous materials for carbon dioxide separations. *Nat. Mater.* **20**, 1060–1072 (2021).
15. M. Erans *et al.*, Direct air capture: Process technology, techno-economic and socio-political challenges. *Energy Environ. Sci.* **15**, 1360–1405 (2022).
16. Y. Belmabkhout, V. Guillerm, M. Eddaoudi, Low concentration CO_2 capture using physical adsorbents: Are metal–organic frameworks becoming the new benchmark materials? *Chem. Eng. J.* **296**, 386–397 (2016).
17. O. Shekhah *et al.*, Made-to-order metal-organic frameworks for trace carbon dioxide removal and air capture. *Nat. Commun.* **5**, 4228 (2014).
18. S. Mukherjee *et al.*, Trace CO_2 capture by an ultramicroporous physisorbent with low water affinity. *Sci. Adv.* **5**, eaax9171 (2019).
19. P. Nugent *et al.*, Porous materials with optimal adsorption thermodynamics and kinetics for CO_2 separation. *Nature* **495**, 80–84 (2013).
20. A. Kumar *et al.*, Hybrid ultramicroporous materials (HUMs) with enhanced stability and trace carbon capture performance. *Chem. Commun. (Camb.)* **53**, 5946–5949 (2017).
21. E. M. Flanigen, R. W. Broach, S. T. Wilson, "Introduction" in *Zeolites in Industrial Separation and Catalysis*, S. Kulprathipanja, Ed. (Wiley-VCH, Weinheim, 2010), pp. 1–26.
22. N. R. Stuckert, R. T. Yang, CO_2 capture from the atmosphere and simultaneous concentration using zeolites and amine-grafted SBA-15. *Environ. Sci. Technol.* **45**, 10257–10264 (2011).
23. H. J. Choi, D. Jo, J. G. Min, S. B. Hong, The origin of selective adsorption of CO_2 on merlinoite zeolites. *Angew. Chem. Int. Ed. Engl.* **60**, 4307–4314 (2021).
24. M. M. Lozinska *et al.*, Understanding carbon dioxide adsorption on univalent cation forms of the flexible zeolite Rho at conditions relevant to carbon capture from flue gases. *J. Am. Chem. Soc.* **134**, 17628–17642 (2012).
25. S. E. Jee, D. S. Sholl, Carbon dioxide and methane transport in DDR zeolite: Insights from molecular simulations into carbon dioxide separations in small pore zeolites. *J. Am. Chem. Soc.* **131**, 7896–7904 (2009).
26. G. E. Cmarik, J. C. Knox, "CO_2 removal for the international space station – 4-Bed Molecular Sieve material selection and system design" in *49th Int. Conf. Environ. Syst.* (2019), pp. 1–10.
27. S. M. W. Wilson, F. H. Tezel, Direct dry air capture of CO_2 using VTSA with faujasite zeolites. *Ind. Eng. Chem. Res.* **59**, 8783–8794 (2020).
28. D. Fu, Y. Park, M. E. Davis, Zinc containing small-pore zeolites for capture of low concentration carbon dioxide. *Angew. Chem. Int. Ed. Engl.* **61**, e202112916 (2022).
29. S. Liu *et al.*, Regulating extra-framework cations in faujasite zeolites for capture of trace carbon dioxide. *Chemistry* **28**, e202201659 (2022).
30. A. Oda *et al.*, Unprecedented CO_2 adsorption behaviour by 5A-type zeolite discovered in lower pressure region and at 300 K. *J. Mater. Chem. A Mater. Energy Sustain.* **9**, 7531–7545 (2021).
31. S. Choi, J. H. Drese, C. W. Jones, Adsorbent materials for carbon dioxide capture from large anthropogenic point sources. *ChemSusChem* **2**, 796–854 (2009).
32. S. U. Rege, R. T. Yang, M. A. Buzanowski, Sorbents for air prepurification in air separation. *Chem. Eng. Sci.* **55**, 4827–4838 (2000).
33. L. Zhang *et al.*, Crystallization and morphology of mordenite zeolite influenced by various parameters in organic-free synthesis. *Mater. Res. Bull.* **46**, 894–900 (2011).
34. P. Cheung, A. Bhan, G. J. Sunley, E. Iglesia, Selective carbonylation of dimethyl ether to methyl acetate catalyzed by acidic zeolites. *Angew. Chem. Int. Ed. Engl.* **45**, 1617–1620 (2006).
35. A. Bhan, A. D. Allian, G. J. Sunley, D. J. Law, E. Iglesia, Specificity of sites within eight-membered ring zeolite channels for carbonylation of methyls to acetyls. *J. Am. Chem. Soc.* **129**, 4919–4924 (2007).
36. R. Gounder, E. Iglesia, Catalytic consequences of spatial constraints and acid site location for monomolecular alkane activation on zeolites. *J. Am. Chem. Soc.* **131**, 1958–1971 (2009).
37. F. Jiao *et al.*, Shape-selective zeolites promote ethylene formation from syngas via a ketene intermediate. *Angew. Chem. Int. Ed. Engl.* **57**, 4692–4696 (2018).
38. Y. Zhou *et al.*, Self-assembled iron-containing mordenite monolith for carbon dioxide sieving. *Science* **373**, 315–320 (2021).
39. Z.-M. Wang, T. Arai, M. Kumagai, Adsorption separation of low concentrations of CO_2 and NO_2 by synthetic zeolites. *Energy Fuels* **12**, 1055–1060 (1998).
40. K. Yamashita *et al.*, Synthetic and natural MOR zeolites as high-capacity adsorbents for the removal of nitrous oxide. *Chem. Commun. (Camb.)* **57**, 1312–1315 (2021).
41. Y. Román-Leshkov, M. Moliner, M. E. Davis, Impact of controlling the site distribution of Al atoms on catalytic properties in ferrierite-type zeolites. *J. Phys. Chem. C* **115**, 1096–1102 (2011).
42. Z. Cheng *et al.*, Role of brønsted acid sites within 8-MR of mordenite in the deactivation roadmap for dimethyl ether carbonylation. *ACS Catal.* **11**, 5647–5657 (2021).
43. X. Luo *et al.*, Significant improvements in CO_2 capture by pyridine-containing anion-functionalized ionic liquids through multiple-site cooperative interactions. *Angew. Chem. Int. Ed. Engl.* **53**, 7053–7057 (2014).
44. P. E. Hathaway, M. E. Davis, High resolution, quasi-equilibrium sorption studies of molecular sieves. *Catal. Lett.* **5**, 333–347 (1990).
45. V. M. Georgieva *et al.*, Triggered gate opening and breathing effects during selective CO_2 adsorption by merlinoite zeolite. *J. Am. Chem. Soc.* **141**, 12744–12759 (2019).
46. B. Bonelli, B. Onida, B. Fubini, C. O. Areán, E. Garrone, Vibrational and thermodynamic study of the adsorption of carbon dioxide on the zeolite Na—ZSM-5. *Langmuir* **16**, 4976–4983 (2000).
47. M. Boronat, C. Martínez-Sánchez, D. Law, A. Corma, Enzyme-like specificity in zeolites: A unique site position in mordenite for selective carbonylation of methanol and dimethyl ether with CO. *J. Am. Chem. Soc.* **130**, 16316–16323 (2008).
48. L. Grajciar *et al.*, Controlling the adsorption enthalpy of $CO(_2)$ in zeolites by framework topology and composition. *ChemSusChem* **5**, 2011–2022 (2012).
49. B. K. Singh *et al.*, Template free facile synthesis of mesoporous mordenite for bulky molecular catalytic reactions. *J. Ind. Eng. Chem.* **57**, 363–369 (2018).
50. T. D. Pham, R. Xiong, S. I. Sandler, R. F. Lobo, Experimental and computational studies on the adsorption of CO_2 and N_2 on pure silica zeolites. *Microporous Mesoporous Mater.* **185**, 157–166 (2014).
51. J. W. Ward, H. W. Habgood, The infrared spectra of carbon dioxide adsorbed on zeolite X. *J. Phys. Chem.* **70**, 1178–1182 (1966).
52. D. Fu, Y. Park, M. E. Davis, Single crystal CIF files for Confinement Effects Facilitate Low Concentration Carbon Dioxide Capture with Zeolites. CaltechDATA. https://data.caltech.edu/records/20259. Deposited 10 August 2022.